



Hydrogen diffusivity measurement and microstructural characterization of Custom 465 stainless steel



S. Ifergane^{a,b}, E. Sabatani^b, B. Carmeli^b, Z. Barkay^c, V. Ezersky^d, O. Beeri^b, N. Eliaz^{a,*}

^a Department of Materials Science and Engineering, Tel-Aviv University, Ramat Aviv, Tel Aviv 6997801, Israel

^b Nuclear Research Center Negev, Beer Sheva, Israel

^c The Wolfson Applied Materials Research Centre, Tel-Aviv University, Ramat Aviv, Tel Aviv 6997801, Israel

^d Ilse Katz Institute for Nanoscale Science and Technology, Ben-Gurion University, Beer-Sheva, Israel

ARTICLE INFO

Article history:

Received 10 March 2015

Received in revised form 4 August 2015

Accepted 4 August 2015

Available online 7 August 2015

Keywords:

Hydrogen diffusion

Hydrogen permeation

Effects of strain

Precipitation hardening stainless steel

Custom 465

ABSTRACT

Hydrogen diffusivity in Custom 465[®] martensitic precipitation hardened stainless steel is determined using electrochemical permeation tests. Hydrogen diffusivity in the solution annealed (SA) condition is approximately 10 times higher than in the aged H900 (480 °C, 4 h) condition because of hydrogen traps such as Ni₃Ti nano-precipitates and reverted austenite. The microstructure of the alloy is characterized by TEM, XRD and ESEM/EBSD, both in the aged H900 and in the SA conditions. In the aged condition, η-Ni₃Ti nano-precipitates with hexagonal structure and a rod-like shape are observed. In addition, reverted austenite is found at grain boundaries and inter-lath interfaces. In the SA condition, these microstructural features are not evident, which may explain the higher diffusivity measured. The diffusivity is almost unaffected by prior microplastic deformation of H900.

© 2015 Elsevier Ltd. All rights reserved.

1. Introduction

Carpenter Technology's Custom 465[®] stainless steel (UNS S46500) [1–3] is a martensitic, age-hardenable alloy that offers a unique combination of high strength, toughness, and corrosion resistance. An ultimate tensile strength higher than 250 ksi (1722 MPa) can be obtained following aging at 482 °C (the H900 condition). However, the H900 condition is characterized by higher susceptibility to corrosion and stress corrosion cracking (SCC) compared to other conditions associated with aging at higher temperatures [4,5].

The microstructure of Custom 465[®] stainless steel in the solution annealed (SA) condition consists of Fe-Ni lath martensite (BCC phase) [6–7]. As reported for other precipitation hardened stainless steels [8–11], large prior austenite grains are divided into “packets” that are subdivided into “blocks” of martensite laths. When an austenite grain shears under martensitic transformation, there are altogether 24 potential orientations of martensite (variants) that are formed from a single austenite grain. Each packet of lamellae is actually a single martensite variant.

For Custom 465[®] stainless steel it was reported [6–7] that during the aging treatments, η-Ni₃Ti coherent nano-precipitates

are formed inside the martensite lamellae. Reverted austenite is formed between lamella, although its amount was not quantified. The precipitation behavior and the strengthening mechanism in other corrosion-resistant maraging steels have been investigated [12–13]. η-Ni₃Ti precipitates have hexagonal crystallographic structure and a rod-like shape. The size of the precipitates is governed by the time and temperature of the aging treatment. Strengthening by η-Ni₃Ti in the early stage of precipitation is due to coherency stresses and internal ordering.

Not much is known about the sensitivity of Custom 465[®] to hydrogen embrittlement (HE). Lee and Gangloff [14] compared this sensitivity to HE of AerMet[™] 100. It was reported that, in the H900 condition, the fracture mode changes from ductile transgranular to intergranular, due to hydrogen charging. Based on trends in other precipitation hardened (PH) stainless steels [15–23], it is speculated that the sensitivity to hydrogen is severe in the H900 condition.

In the current work, we used the electrochemical hydrogen permeation technique [24] in order to: (1) Characterize hydrogen diffusivity in Custom 465[®] stainless steel. (2) Compare between specimens in the SA condition and in the aged H900 condition, in order to determine the effect of aging on hydrogen diffusivity. (c) Study the effect of prior deformation, which is common in high-stress engineering applications, on hydrogen permeation.

* Corresponding author.

E-mail address: neliaz@tau.ac.il (N. Eliaz).

2. Experimental procedure

2.1. Thermomechanical treatments and microstructure characterization of Custom 465[®]

Custom 465[®] stainless steel in the form of a 2-inch diameter rod was purchased from Carpenter Technology (Wyomissing, PA, USA). The composition of this steel (wt.%) was determined by Inductively Coupled Plasma Atomic Emission Spectroscopy (ICP-AES) analysis as: Fe–10.7Cr–10.9Ni–0.86Mo–1.4Ti–0.04Al–0.04Zn–0.0046C. The rod was received in the SA and cold-treated condition. The SA treatment was done at 982°C for 1 h, followed by rapid cooling to room temperature in either air or a liquid coolant. A subzero cooling at –73°C for 8 h within 8 h from the SA treatment is essential for optimal aging response [3]. Specimens were cut in the transverse direction. Three specimen types were tested: (1) **SA**: Solution annealed condition, (2) **H900**: Aged at 482°C for 4 h in argon shielding atmosphere, followed by cooling in argon, and (3) **deformed H900**: simulating prior deformation effects of already aged components in service. These specimens were aged to H900 and afterwards were subjected to 0.18–0.23% uniaxial deformation, which is close to the yield point in the microplastic deformation region. The degree of deformation was evaluated by a finite element analysis model, in which the plastic strain field generated in uniaxial tension of thin sheet specimen was computed using ABAQUS/explicit 6.1 software.

The microstructure was characterized by scanning electron microscope (SEM), electron backscattered diffraction (EBSD), and X-ray diffraction (XRD). Specimens were ground on SiC papers down to 600 grit, followed by polishing down to 1 μm using diamond polish paste. For metallographic characterization, chemical etching was done by immersion in Vilella's reagent, which consists of 5 mL HCl + 2 g picric acid + 100 mL methyl alcohol. For EBSD examinations, specimens were prepared by polishing with colloidal silica to remove the stressed surface layer, followed by electrochemical etching in 64% phosphoric acid + 15% sulfuric acid + 21% water (volume percentages) solution at 3 V for 2 s.

SEM examination was done by Quanta 200 FEG ESEM from FEI. For EBSD analyses, a HKL-Oxford Channel 5 system with Nordlys II detector was used. The following operation conditions were maintained: working distance 15 mm, inclination relative to the main beam 70°.

Three specimens from each type were characterized by XRD, each specimen was tested three times: before hydrogen charging, immediately after charging, and one day later. XRD patterns were acquired 1 h after the end of the electrochemical permeation test, thus ensuring that the specimens were still charged with hydrogen. Data were collected on Panalytical Empyrean Powder Diffractometer equipped with a position sensitive (PSD) PIXCEL detector and a graphite monochromator on the diffracted beam providing Cu-Kα radiation. The operation conditions were: 40 kV and 30 mA. The Bragg-Brentano diffractometer was employed. $\theta/2\theta$ scans were run for 30 min in a 2θ range of 40–95 deg with steps equal to ~ 0.033 deg. The relative quantities of reverted austenite were analyzed by Rietveld analysis using FullProof software.

Samples for transmission electron microscopy (TEM) study were mechanically polished to a 100-μm thickness on a 1000 grit SiC grinding paper and polished with 6 μm and 1 μm diamond pastes. The central area of the disk sample was dimple grinded to 20 μm thickness and then ion-milled to electron transparency using Gatan precision ion polishing system (PIPS). TEM and selected area electron diffraction (SAED) experiments were carried out in a JEOL JEM-2100F TEM equipped with an energy-dispersive X-ray spectrometer (EDS) system model JED 2300T. The acquisition

parameters were: probe size of 1 nm, acquisition time 20 s, 138 eV resolution.

2.2. Electrochemical hydrogen permeation tests

Electrochemical hydrogen permeation tests were performed in order to determine the diffusion coefficient, permeability and hydrogen subsurface concentration for a given charging condition. The technique was developed by Devanathan and Stachurski [24], and later described in detail elsewhere [25–28]. The experimental setup is described in Fig. 1a. It is comprised of a two-compartment cell, with the specimen being a membrane separating the two compartments. System validation was done with Pd–0.1 wt.%Pt specimens, comparing the results to reported values [29].

For the permeation tests, specimens were ground to a thickness of 0.125–0.2 mm in the same manner described above. The proper specimen thickness range was determined empirically. For too high specimen thicknesses, the experiment durations are too long. On the other hand, an insufficient thickness does not comply with the required thickness of at least 5 grains or packets of banded martensite [24]. In a case where this requirement is not complied with, hydrogen may diffuse through grain boundaries, bypassing transport through the grains. In order to avoid edge effects that cause significant hydrogen leakage laterally, the L/r ratio (where L is the membrane thickness and r is the radius of the surface area exposed to the catholyte) was kept below 0.03. For a reliable measurement, with minimal leakage, this ratio should be less than 0.05 [24,25]. For each sample type, three specimens were tested in various thicknesses, in order to avoid surface and undesired size effects [24].

In the final preparation step prior to the onset of the permeation test, the surface oxide film was removed by polishing with a 1-μm diamond paste. Afterwards, specimens were rinsed in detergent, washed in water, ultrasonically cleaned in acetone, dried quickly in high-pressure air stream, washed in ethanol, and dried in high-

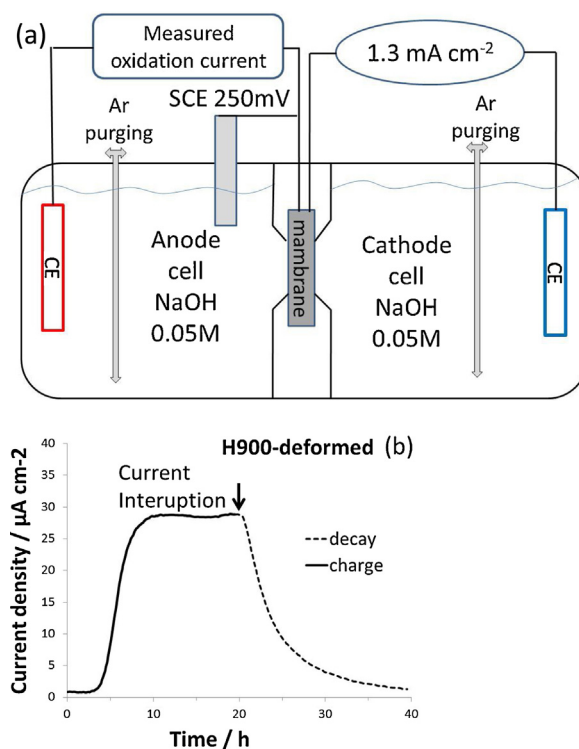


Fig. 1. (a) Schematic illustration of the electrochemical permeation cell assembly. (b) Electrochemical hydrogen permeation charging and decay transients.

pressure room temperature air. Following surface activation in a 0.5 M HF + 2.5 M HNO₃ aqueous solution for 10 s and water rinse, the specimens were electrochemically coated on both sides with a palladium thin layer with a thickness of 4±1 nm. The palladium thickness was determined by electrochemical stripping in a 0.1 M H₂SO₄ + 0.02 M KCl solution.

During hydrogen charging, the hydrogen entry (cathodic) side was galvanostatically polarized at a constant current density of 1.3 mA cm⁻² in 0.05 M NaOH solution. During decay (discharge), the cathodic current was terminated. During the entire permeation experiment, the hydrogen exit (anodic) side was held at a constant potential of +0.25 V vs. Saturated Calomel Electrode (SCE) in a 0.05 M NaOH solution, and the resulting anodic current was recorded using a PGSTAT30 Autolab potentiostat. Argon gas was purged for 30 min prior to cathodic polarization and during the entire experiment to remove oxygen. The measured anodic current is a direct measurement of hydrogen flow rate out of the specimen. During charging, the anodic current rose until a steady-state was reached, whereas during discharge the current decayed until the background oxidation current measured was practically zero, namely under 0.1 μA cm⁻² [27]. For each specimen, the experiment was performed until at least three consecutive charging-decay cycles exhibited repeatable rise and decay transients. All tests were performed at room temperature. A typical complete charging-discharging cycle is illustrated in Fig. 1b.

It is common to associate the effective diffusion coefficient D_{eff} with the experimentally determined $D_{lag_63\%}$ (for charging):

$$D_{lag_63\%} = \frac{L^2}{6t_{lag_63\%}} \quad (1)$$

where L is the thickness of the specimen, $t_{lag_63\%}$ is the time during charging transient when the current density (j) reaches 63% of the final steady-state current density (j_{max}).

When steady state is achieved during charging, the hydrogen concentration distribution across the specimen is assumed to be linear [25]:

$$C(0, x) = C_0 \left(1 - \frac{x}{L}\right) \quad (2)$$

where C_0 is the subsurface concentration of atomic hydrogen in interstitial lattice sites on the charging side of the sample (mol m⁻³) [26].

When only reversible trapping is important and the permeation transient can be represented by Fick's second law, the sum of the subsurface concentration of hydrogen in interstitial lattice sites and reversible trap sites on the charging side of the sample, C_{OR} , can

be calculated from the following equation [26,30]:

$$J_{ss} = \frac{D_{eff}}{L} C_{OR} \quad (3)$$

J_{ss} , the permeation flux of hydrogen at steady-state as measured on the exit (oxidation) side of the membrane (mol cm⁻² s⁻¹) is obtained from the maximal current density j_{max} , using the relation $J_{ss} = j_{max}/nF$, where nF is the charge transferred per 1 mol of H.

3. Results

3.1. The microstructure of Custom 465[®]

In all three thermomechanical conditions (SA, aged H900 and H900+deformed, see Section 2.1), Fe-Ni banded martensite with BCC structure was observed by SEM metallography (Fig. 2) and EBSD analyses (Fig. 3). The misorientation angle between lamellae inside the packet is 60° (yellow color in Fig. 3a,b). Prior austenitic grain boundaries and boundaries between packets and blocks are at lower misorientation angles, around 45° (white color in Fig. 3a,b). It is evident from Fig. 3 that the diameter of grains and packets of laths is about 25 μm. This value would necessitate a minimal specimen thickness of 125 μm for hydrogen permeation tests.

TiN precipitates are arbitrarily distributed. Their size is within the range of 5–10 μm, and the average distance between them is about 100 μm. SEM/EDS analysis of the precipitates reveals only Ti and N, in a 1:1 atomic ratio. Based on EBSD analysis, these are FCC TiN single-crystal precipitates. The TiN phase has been characterized elsewhere [31]. After hydrogen exposure, these precipitates were characterized by SEM/EBSD; phenomena such as cracking or microstructural changes were not evident.

Reverted austenite was observed by XRD (Fig. 4) and EBSD (Fig. 3). The relative quantity of reverted austenite measured by XRD in the aged H900 specimens was 4±1 wt%. Deformation had no effect on the amount of reverted austenite, within the accuracy of the measurement. In the SA condition, a negligible amount of reverted austenite (<1%) was detected.

EBSD revealed the reverted austenite as FCC submicron grains between lamellae (Fig. 3a). In comparison, in PH 13-8Mo H900 martensitic stainless steel, reverted austenite has been observed mainly at martensite interlath boundaries [19,20]. In the aged specimens, the austenite content was similar, about 5.0%, 6.5% and 7.5% for the H875, H950 and H1025 conditions, respectively [18]. For all specimens, the XRD and EBSD patterns did not change after hydrogen permeation tests, either shortly after charging or a day later.

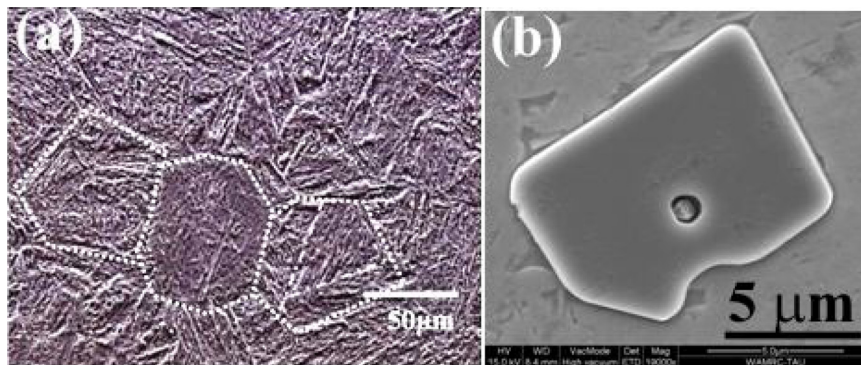


Fig. 2. SEM secondary electron (SE) images of a H900 sample. (a) Metallography after polishing and etching. Prior austenite grain boundaries (dot lines), with packets of banded martensite divided to block boundaries between lamellae (dot-and-dash lines). (b) After polishing only. A TiN precipitate, as determined by SEM/EDS and EBSD analysis.

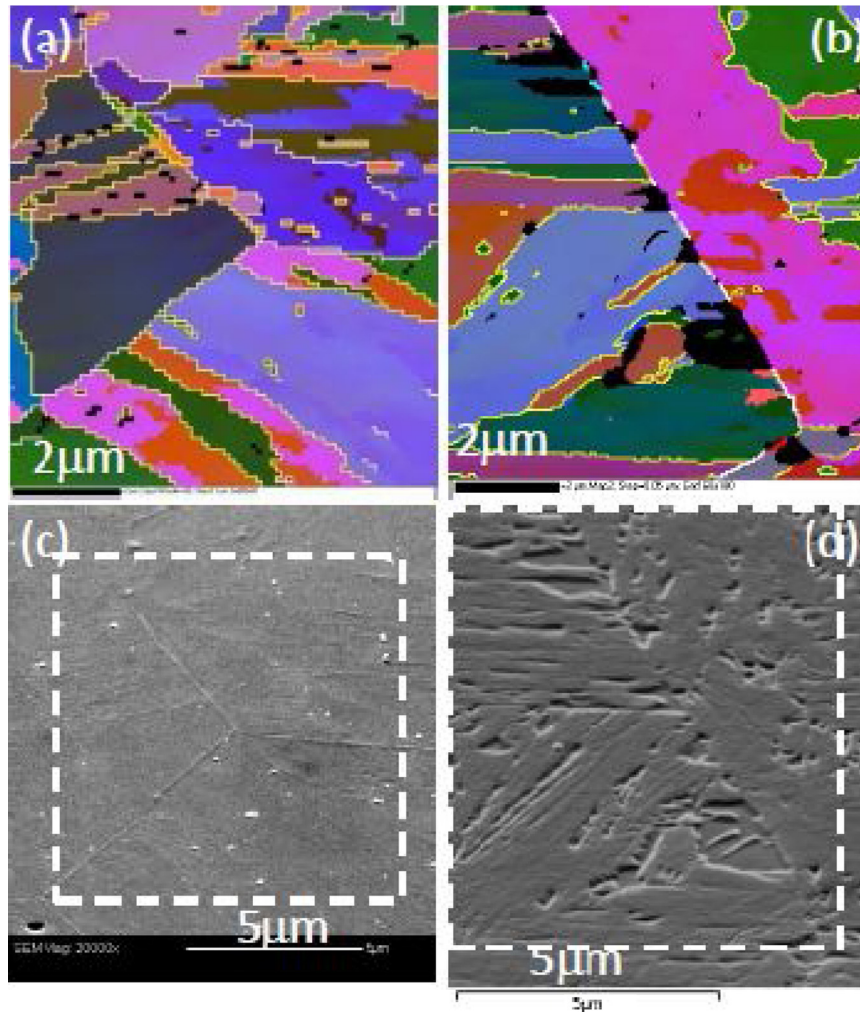


Fig. 3. EBSD images of SA (a) and H900 sample (b). Darker areas are of reverted austenite (FCC), while the remaining areas are of martensite (BCC). 60° interfaces represent interlath boundaries, whereas $20\text{--}55^\circ$ interfaces are related to grain boundaries, packet boundaries and block boundaries. SEM SE-images (tilt of 70°) of SA (c) and H900 (d) samples. The areas within the dashed lines were analyzed by EBSD in figures a and b, respectively.

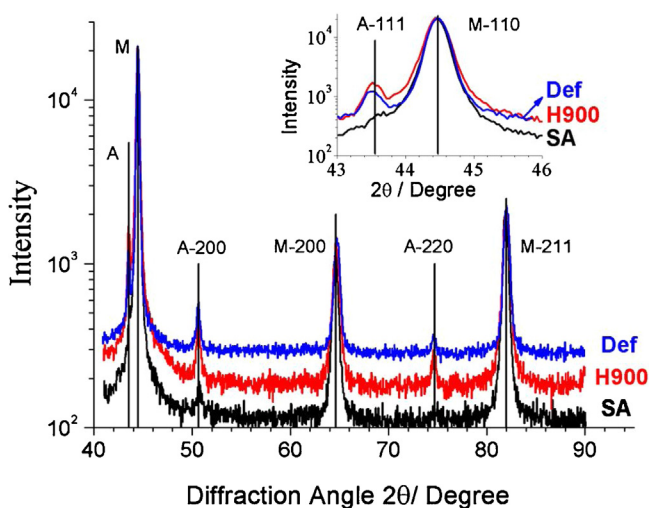


Fig. 4. XRD patterns normalized according to the highest martensite M(110) peak in each pattern. A martensite BCC phase is evident in all three sample types: SA (black), H900 (red) and deformed H900 (blue). (For interpretation of the references to color in this figure legend, the reader is referred to the web version of this article.)

Bright-field TEM image of the as-received specimen and its corresponding SAED pattern are shown in Fig. 5. The alloy is composed of a single-phase martensitic BCC structure. TEM examination of the specimen aged to H900 condition (Fig. 6) revealed the presence of precipitates, as can be concluded from the additional reflections in the SAED pattern, which were found to correspond to Ni_3Ti hexagonal phase. A dark field (DF) image taken from the $(2\bar{2}\bar{4}0)$ Ni_3Ti reflection which is parallel to the long axis of the precipitates revealed rod-shaped precipitates, about 25-nm long and 3 nm in diameter (Fig. 6b). The orientation relationship between the Ni_3Ti precipitates and the martensite matrix was calculated from Fig. 6c as $\{011\}_M // \{0001\}_{\text{Ni}_3\text{Ti}}$ and $\langle 1\bar{1}1 \rangle_M // \langle 11\bar{2}0 \rangle_{\text{Ni}_3\text{Ti}}$. Such relations have been reported for other steels such as maraging T-250 [32,33].

TEM images of the specimen aged for 4 hours at 510°C are shown in Fig. 7. The DF image taken from the $(2\bar{2}\bar{4}0)$ reflection (Fig. 7b) reveals larger precipitates (about 100-nm long and 25 nm in diameter) while retaining their rod-shaped morphology. According to the SAED pattern, the orientation relations with the matrix are maintained. The extended dimensions of the precipitates enabled to perform an EDS analysis at their center (location a in Fig. 7d) and to compare their composition to that of the matrix (location b in Fig. 7d). According to the EDS data (Fig. 8) the relative (Ni + Ti) weight concentration is much higher inside

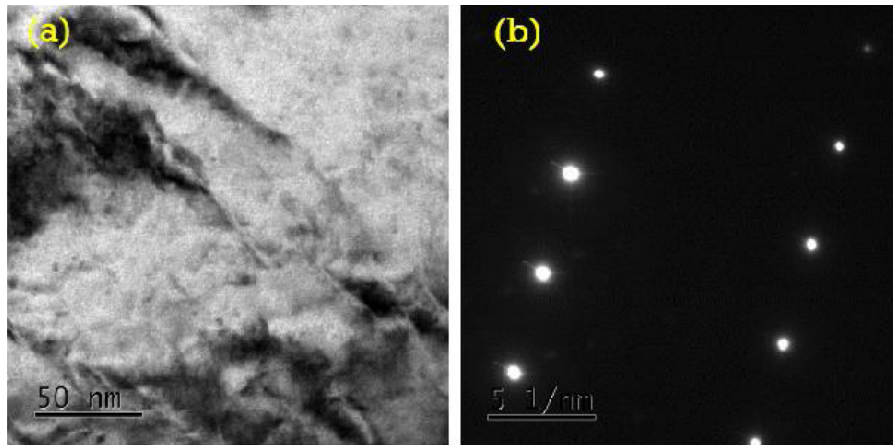


Fig. 5. Custom 465[®] steel in SA condition. BF (a) and SAD (b) micrographs taken from the $[112]_M$ SAD zone axis. No precipitates were observed.

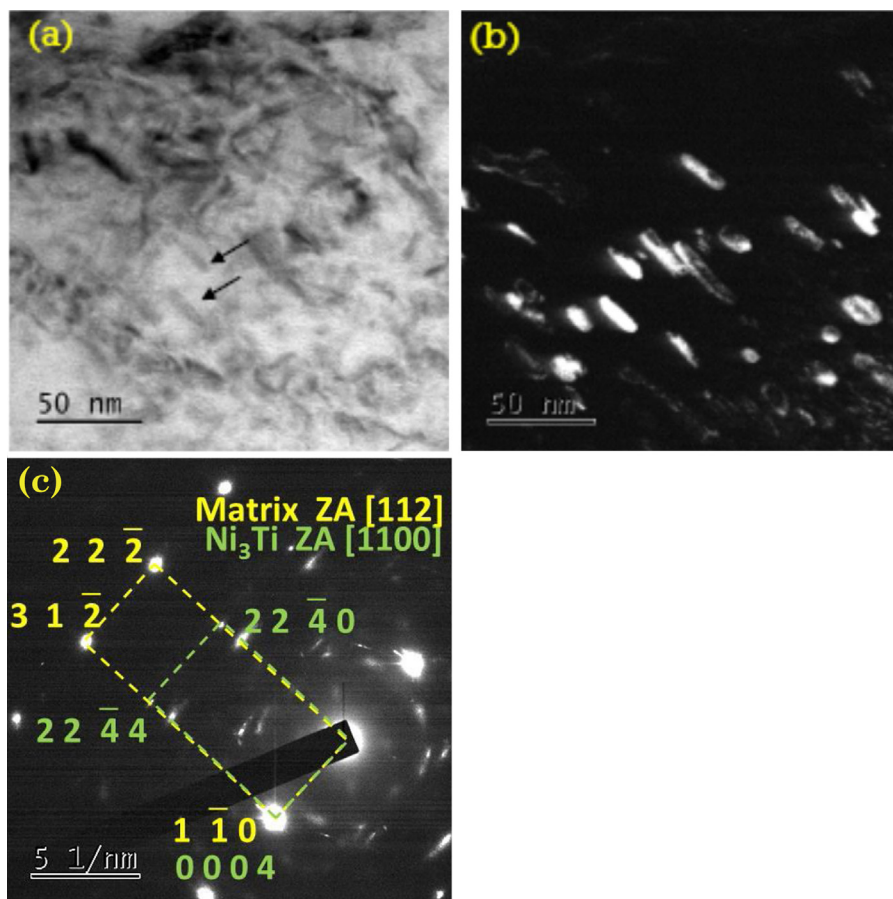


Fig. 6. Custom 465[®] steel, aged at 480°C for 4 h (H900). (a) BF micrograph at zone axis $[112]_M$. (b) DF micrograph taken from the $(22\bar{4}0)$ reflection of Ni_3Ti precipitates. (c) SAD micrograph. Orientation relations between precipitates and matrix are demonstrated.

the precipitate than in the surrounding matrix. Such results were repeated in several measurements. This indicates that the precipitates consist of Ni and Ti.

3.2. Hydrogen permeation tests

Charging and decay transients (oxidation current density versus time) for a representative sample are shown in Figs. 9, 10 and 11 for SA, H900 and H900+deformed conditions, respectively. In Figs. 9–11, the time for charging and for decay

transients is nearly equal for each cycle. In the first three cycles, the charging time in each cycle is shorter than in the preceding cycles. In addition, the steady-state current density in each cycle is higher than in the preceding cycle. The 1st and 2nd cycles in Figs. 9–11 are influenced by high concentration of irreversible traps (including surface and bulk traps) which need time to be saturated with hydrogen [24–27]. It seems that not all irreversible traps were filled during the 1st cycle, because the plateau at the end of the cycle is not perfectly horizontal. However, the 3rd cycle converges with the 4th cycle and on, indicating that irreversible traps were

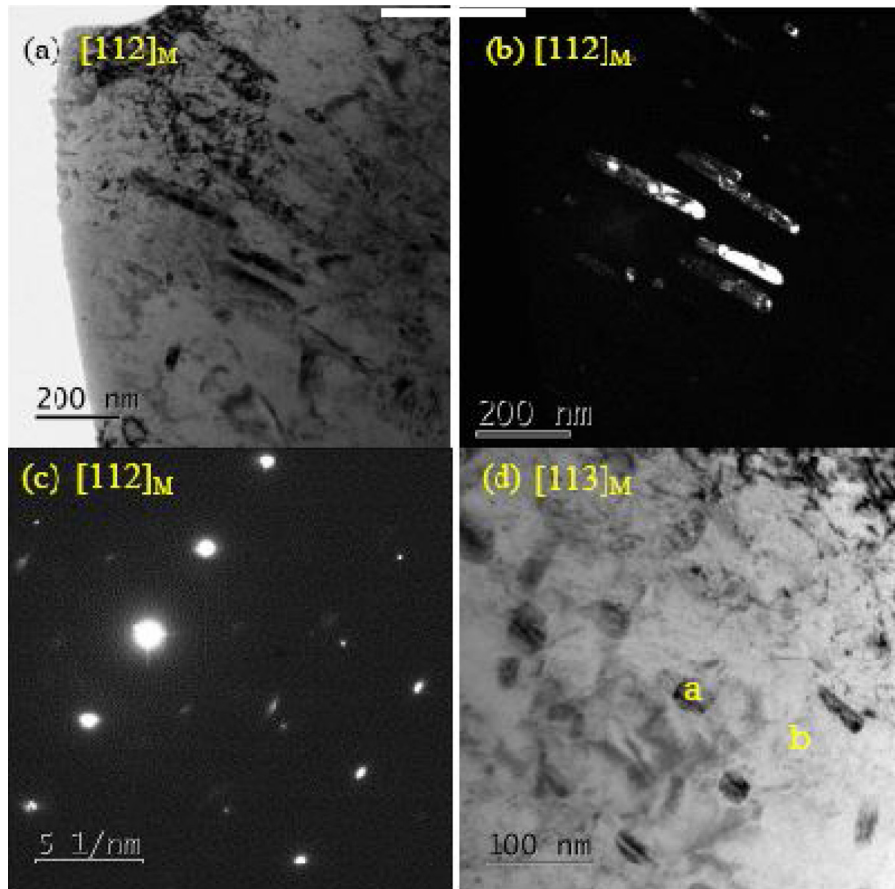


Fig. 7. Custom 465[®] steel aged at 510 °C for 4 h. (a) BF micrograph at zone axis $[112]_M$. (b) DF micrograph taken from the $(22\bar{4}0)$ Ni_3Ti precipitates. (c) Orientation relation between precipitates and matrix, as marked on the $[112]_M$ SAD pattern. (d) Precipitates at zone axis $[113]_M$. EDS data is shown in Fig. 8.

filled after the 2nd cycle. Therefore, calculation of the diffusion coefficients was performed taking into account only permeation transients from the 3rd cycle on, where irreversible traps are practically fully occupied and only reversible traps and lattice hydrogen are expected to play a role.

For each sample type, at least three specimens with different thicknesses were tested. Apparently, undesired surface effects and size effects [27,28] are negligible, as the measured diffusivity is not influenced by the thickness of the specimen. After the permeation test, the surface of the specimens was examined visually as well as by SEM. No change of the specimen surface was detected compared to the surface before the experiment.

Fig. 12 shows the relative position of the steep slope of charging and decay transients, in the normalized current density j/j_∞ versus log of the dimensionless time ($\tau = D_{\text{Fe}}t/L^2$) curves, for representative repeatable cycles for each specimen type (SA, aged H900, H900 + deformation). The diffusivity is clearly affected by the thermo-mechanical conditions of the specimens. The results calculated from such curves are listed in Table 1. The diffusion coefficient ($D_{\text{lag},63\%}$) of the aged H900 samples is approximately 10 times lower than that of the SA samples. Higher values of D_{eff} have been reported for other PH martensitic stainless steels in the SA condition compared to the H900 condition (see Table 1). The diffusion coefficient of H900 + deformed samples is similar to that of H900 samples.

Although experiments with similar sample types did not always yield the same maximum current density, the calculated diffusion coefficients were similar (see Table 1). The variation in current density may be related to variations in hydrogen subsurface concentration, which result from small perturbations in the

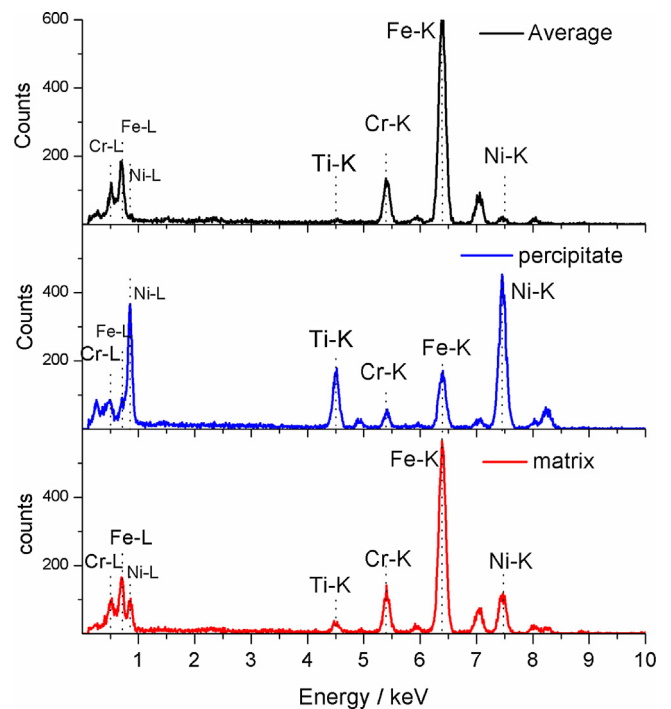


Fig. 8. Custom 465[®] steel aged at 510 °C for 4 h. (a) EDS analyses locations are marked in Fig. 7d. Average analysis was acquired from an arbitrary area of $300 \times 300 \text{ nm}^2$. (b) Point analyses on precipitate marked "a" in Fig. 7d. (c) Nearby matrix analysis marked "b" in Fig. 7d.

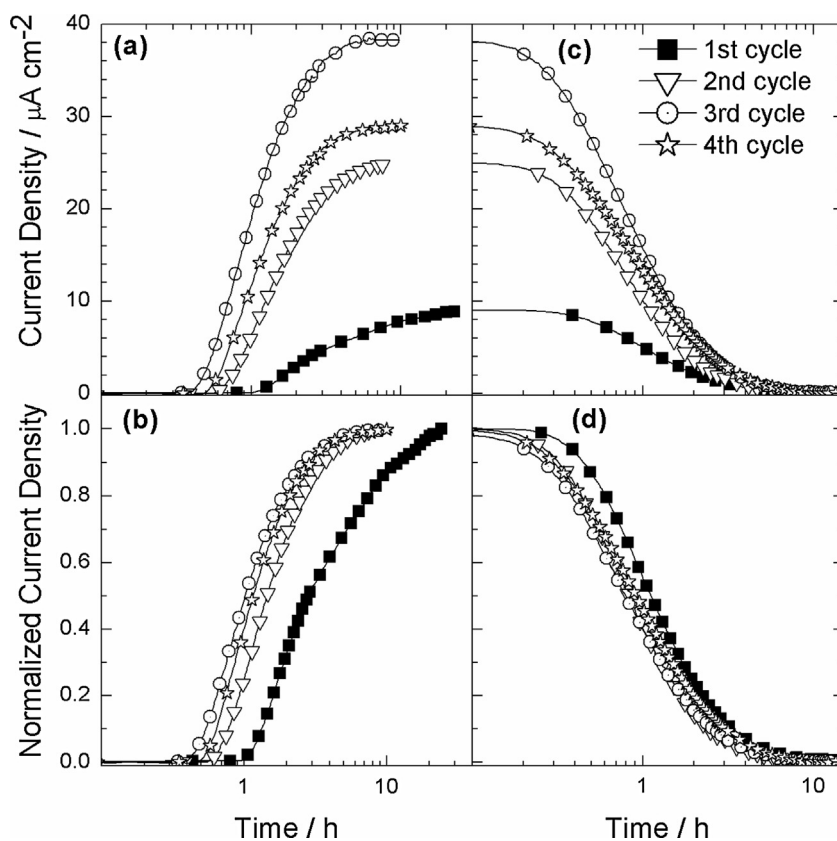


Fig. 9. Electrochemical hydrogen permeation transients for a SA sample, membrane thickness of 180 μm . Charging (a) and decay (b) current densities, and the corresponding charging (c) and decay (d) normalized current densities (j/j_{max}).

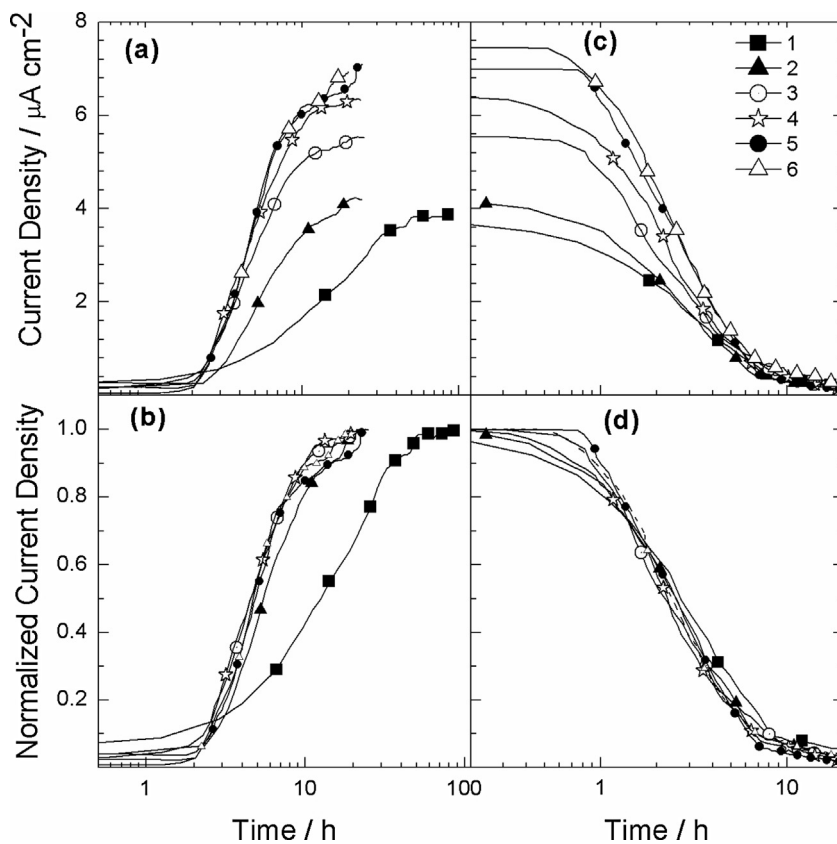


Fig. 10. Electrochemical hydrogen permeation transients for a H900 sample, membrane thickness of 125 μm . Charging (a) and decay (b) current densities, and the corresponding charging (c) and decay (d) normalized current densities (j/j_{max}).

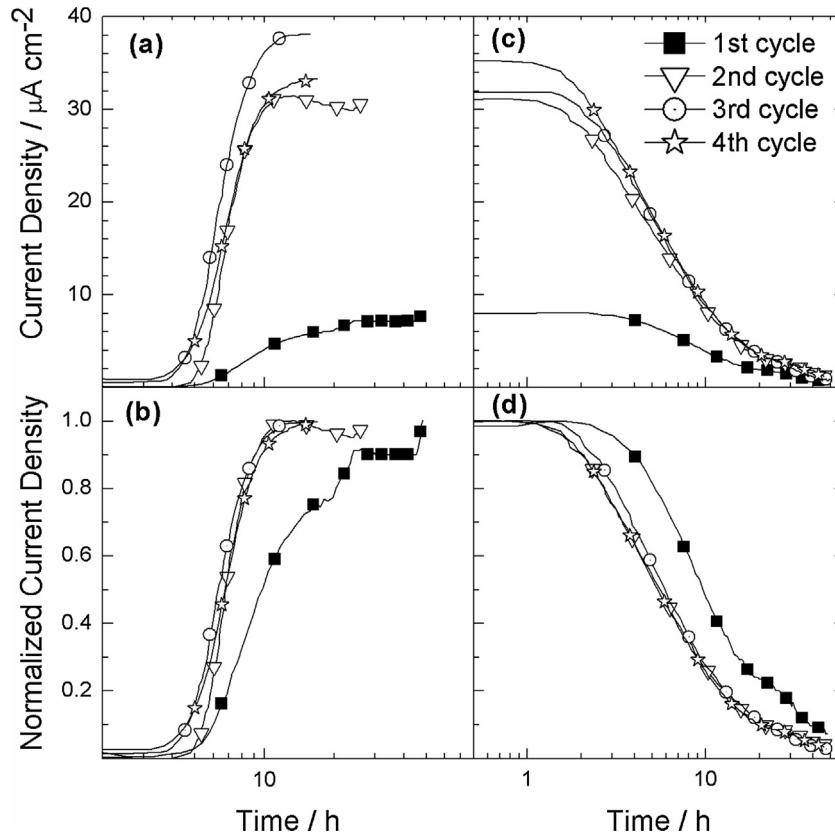


Fig. 11. Electrochemical hydrogen permeation transients for a H900 sample that had undergone prior microplastic deformation, membrane thickness of 160 μm . Charging (a) and decay (b) current densities, and the corresponding charging (c) and decay (d) normalized current densities (j/j_{max}).

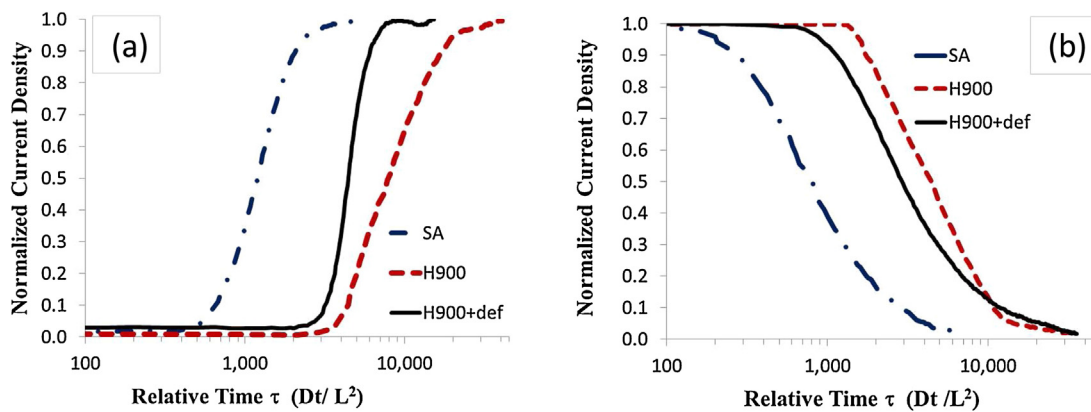


Fig. 12. Normalized current density vs. dimensionless time $\tau = D_{\text{Fe}} t / L^2$, $D_{\text{Fe}} = 7.2 \times 10^{-5} \text{ cm}^2 \text{ s}^{-1}$ [23]. The charging transients (a) and the decay transients (b) of the three sample types.

Table 1

Average and standard deviation values of $D_{\text{lag}_63\%}$ and D_{bt} ($\times 10^{-9} \text{ cm}^2 \text{ s}^{-1}$) for charging transients and of the subsurface concentration of hydrogen in interstitial lattice sites and reversible traps C_{OR} ($\times 10^{-4} \text{ mol cm}^{-3}$) in Custom 465[®] stainless steel. Comparison is made to values reported for other precipitation-hardened martensitic stainless steels.

Steel	Parameter	SA	Aged H900	Aged H900+ deformed
Custom 465 [®]	$D_{\text{lag}_63\%}$	10.5 \pm 2.0	1.8 \pm 0.6	1.8 \pm 0.2
	D_{bt}	10.8 \pm 2.7	1.6 \pm 0.2	1.1 \pm 0.07
	C_{OR}	6.2 \pm 2.2	9.0 \pm 7.0	6.0 \pm 2.0
17-4	D_{eff}	4.6 [16]	2.8 [16]	--
13-8Mo	D_{eff}	55 [20]	24 [19]	--

charging conditions (cathodic current density, gas purging, temperature, impurities in solution, pH, surface condition, etc.), as reported by Turnbull [28]. Comparing aged and deformed H900 samples, one can see that the calculated $D_{\text{lag}_63\%}$ and D_{bt} values for the two sample types are of the same order of magnitude.

4. Discussion

Custom 465[®], similarly to other martensitic precipitation-hardened stainless steels, exhibits low effective diffusion coefficient relative to other non-PH steels with BCC structure, due to higher reversible trap concentration. The main trap types for

hydrogen were identified by microstructural analysis. Some traps are common to the three thermomechanical conditions: grain boundaries, martensite interfaces, lattice imperfections, some of the alloying elements [34–36], and possibly TiN precipitates. The binding energy of hydrogen at grain boundaries, microvoids and dislocations is typically up to 30 kJ mol⁻¹ at room temperature, as determined experimentally for pure iron [36–38]. These traps are regarded as reversible at room temperature. Common precipitates in steel, such as TiC and MnS, which have a higher binding energy towards hydrogen at room temperature, are considered irreversible [35,39–41].

The diffusion coefficient is found herein to be higher by a factor of approximately 10 for the SA condition than for the aged H900 condition. Higher diffusion coefficients in the SA condition than in the H900 condition have been reported for other PH stainless steels [16,19,20]. The retardation of hydrogen permeation in aged PH stainless steels is related to a larger reversible trapping capacity and can be attributed to: (a) coherent Ni₃Ti nano-precipitates, as reported for Ni₃Mo and possibly Ni₃Ti or FeTi in other PH stainless steels [42]. (b) Reverted austenite, which is formed as thin particles between lamellae and grain boundaries [20,43]. Austenite/martensite interfaces might play a role as reversible traps, just as reported for austenite/ferrite interfaces [44]. For example, it is reported that for 13–8Mo PH stainless steel in the H1100 aging condition, the amount of the reverted austenite increases and the effective diffusion coefficient decreases by an order of magnitude compared to the H900 aging conditions [20].

Deformation in the microplasticity domain of the stress-strain curves of aged H900 samples almost does not change the effective diffusion coefficients during the charging transient. Microplastic deformation is defined as a transitional region between purely elastic and macroplastic deformation and involves limited movement of dislocations and other lattice imperfections. Fast diffusion paths through lattice imperfections and dislocations in the deformed region may enhance diffusivity. On the other hand, deformed regions may contain more traps for hydrogen, which are expected to slow down the diffusivity. These competing phenomena affect the effective diffusion coefficients simultaneously.

Contradicting reports on the effect of deformation on hydrogen diffusivity have been published recently. A slight increase in diffusivity for microplastically deformed material was reported by Hutchings and Turnbull [45] for 410 stainless steel (BCC). In specimens with up to 1.5% deformation, the measured diffusion times were smaller relative to those of undeformed samples. In specimens with 2.1% deformation and more, higher diffusion times were measured relative to undeformed samples. In nickel (FCC), the phenomenon of increased diffusivity in the microplastic deformation region was termed “pipe diffusion” [46]. Similar slight increase of diffusivity by cold-work was observed for 1% deformed 3Cr–1Mo–V bainitic steel [47]. Further deformation up to 5%, which is slightly below the ultimate tensile stress (UTS), resulted in a decrease of the diffusion coefficient. For tempered Fe–C–Cr martensitic steel under stress [48], there was no apparent change in the diffusion coefficient in the elasticity region of the stress-strain curve, but the diffusion coefficient decreased under further plastic deformation up to the UTS.

5. Conclusions

Electrochemical hydrogen permeation tests were used to determine the diffusivity of hydrogen in Custom 465[®] martensitic precipitation hardened stainless steel. The diffusivity of hydrogen in the solution annealed condition was approximately 10 times higher than in the aged condition due to the formation of traps such as hexagonal η-Ni₃Ti nano-precipitates and reverted austenite at grain boundaries and inter-lath interfaces. The

diffusivity was almost unaffected by prior microplastic deformation.

Acknowledgements

This work was supported by Grant No. 205-13 from the Pazy foundation. We thank Profs. Eliezer Gileadi and Amit Kohn for their guidance and helpful comments. We thank Shlomo Levi for his contributions and technical assistance.

References

- [1] H. Raposo, *Stainless steels for small-diameter applications*, *Adv. Mater. Proc.* 167 (2009) 23–24.
- [2] D.E. Wert, R.P. DiSabella, Strong, *corrosion-resistant stainless steel*, *Adv. Mater. Proc.* 164 (2006) 34–36.
- [3] E.U. Lee, R. Goswami, M. Jones, A.K. Vasudevan, *Environment-assisted cracking in Custom 465 stainless steel*, *Metall. Mater. Trans. A* 42 (2011) 415–423.
- [4] C.S. Carter, D.G. Farwick, A.M. Ross, J.M. Uchida, *Stress corrosion properties of high-strength precipitation hardening stainless steels*, *Corrosion* 27 (1971) 190–197.
- [5] D.E. Wert, T.N. Werley, *Comparison of stress corrosion cracking and hydrogen embrittlement resistance of high strength aerospace alloys*, In 2010 TMS Annual Meeting and Exhibition - Supplemental Proceedings 3 (2010) 673–680.
- [6] J.-Y. Chen, J. Liu, Z.-Y. Yang, Y.-Q. Zhang, *Research on precipitates and relationship with martensite of maraging stainless steel*, *Iron Steel (Peking)* 43 (2008) 81–85.
- [7] J.-Y. Chen, Z.-Y. Yang, Y.-Q. Zhang, *Influence of cold deformation on structure and behavior of Custom 465[®]*, *J. Iron Steel Res.* 20 (2008) 31–37.
- [8] T. Maki, *Recent advances in understanding martensite in steel*, In T. Furuhara and K. Tsuzaki (Eds.), *The 1st Int. Symp. On Steel Science*, The Iron and Steel Institute of Japan (2007) 1–10.
- [9] B. Sonderegger, S. Mitsche, H. Cerjak, *Martensite laths in creep resistant martensitic 9–12% Cr steels – Calculation and measurement of misorientations*, *Mater. Charact.* 58 (2007) 874–882.
- [10] V. Seetharaman, M. Sundararaman, R. Krishnan, *Precipitation hardening in PH13–8 Mo stainless steel*, *Mater. Sci. Eng.* 47 (1981) 1–11.
- [11] J.I. Suk, S.H. Hong, S.W. Nam, *Crystallographic orientation relationships among η-Ni₃Ti precipitate, reverted austenite, and martensitic matrix in Fe-10Cr-10Ni-2W maraging alloy*, *Metall. Trans. A* 24 (1993) 2643–2652.
- [12] M. Schober, R. Schnitzler, H. Leitner, *Precipitation evolution in a Ti-free and Ti-containing stainless maraging steel*, *Ultramicroscopy* 109 (2009) 553–562.
- [13] W. Sha, A. Cerezo, G.D.W. Smith, *Phase chemistry and precipitation reactions in maraging steels: Part IV. Discussion and conclusions*, *Metall. Trans. A* 24 (1993) 1251–1256.
- [14] Y. Lee, R.P. Gangloff, *Measurement and modeling of hydrogen environment-assisted cracking of ultra-high-strength steel*, *Metall. Mater. Trans. A* 38 (2007) 2174–2190.
- [15] G.T. Murray, H.H. Honegger, T. Mousel, *Hydrogen embrittlement of PH13–8Mo stainless steel – The effect of surface condition*, *Corrosion* 40 (1984) 146–151.
- [16] W.C. Chiang, C.C. Pu, B.L. Yu, J.K. Wu, *Hydrogen susceptibility of 17–4PH stainless steel*, *Mater. Lett.* 57 (2003) 2485–2488.
- [17] L.M. Young, M.R. Eggleston, H.D. Solomon, L.R. Kaisand, *Hydrogen-assisted cracking in a precipitation-hardened stainless steel: Effects of heat treatment and displacement rate*, *Mater. Sci. Eng. A* 203 (1995) 377–387.
- [18] P. Munn, B. Andersson, *Hydrogen embrittlement of PH13–8Mo steel in simulated real-life tests and slow stain rate tests*, *Corrosion* 46 (1990) 286–295.
- [19] L.W. Tsay, M.Y. Chi, H.R. Chen, C. Chen, *Investigation of hydrogen sulfide stress corrosion cracking of PH 13–8-Mo stainless steel*, *Mater. Sci. Eng. A* 416 (2006) 155–160.
- [20] L.W. Tsay, M.Y. Chi, Y.F. Wu, J.K. Wu, D.Y. Lin, *Hydrogen embrittlement susceptibility and permeability of two ultrahigh strength steels*, *Corros. Sci.* 48 (2006) 1926–1938.
- [21] G.T. Murray, *Hydrogen embrittlement of 15–5PH stainless steel*, *Metall. Trans. A* 12 (1981) 2138–2141.
- [22] B.G. Pound, *Hydrogen trapping in high-strength steels*, *Acta Mater.* 46 (1998) 5733–5746.
- [23] A. Turnbull, M.W. Carroll, D.H. Ferriss, *Analysis of hydrogen diffusion and trapping in a 13% chromium martensitic stainless steel*, *Acta Metall.* 37 (1989) 2039–2046.
- [24] M.A.V. Devanathan, Z. Stachurski, *The adsorption and diffusion of electrolytic hydrogen in palladium*, *Proc. R. Soc. London A* 270 (1962) 90–102.
- [25] ASTM G148–97: *Standard practice for evaluation of hydrogen uptake, permeation, and transport in metals by an electrochemical technique*. ASTM International: 2003.
- [26] BS EN ISO 17081:2014E: *Method of measurement of hydrogen permeation and determination of hydrogen uptake and transport in metals by an electrochemical technique*. ISO: 2014.

- [27] R.N. Iyer, H.W. Pickering, Mechanism and kinetics of electrochemical hydrogen entry and degradation of metallic systems, *Ann. Rev. Mater. Sci.* 20 (1990) 299–338.
- [28] A. Turnbull, Standardisation of hydrogen permeation measurement by the electrochemical technique, In A. Turnbull (Ed.), *Hydrogen Transport and Cracking in Metals*, UK (1994) 129–141.
- [29] V. Berger, E. Gileadi, Adsorption and absorption of hydrogen in palladium, *Electrochim. Acta* 16 (1971) 177–190.
- [30] A.J. Griffiths, A. Turnbull, On the effective diffusivity of hydrogen in low alloy steels, *Corros. Sci.* 37 (1995) 1879–1881.
- [31] H.A. Wriedt, J.L. Murray, The N-Ti (nitrogen-titanium) system, *Bull. Alloy Phase Diagrams* 8 (1987) 378–388.
- [32] V.K. Vasudevan, S.J. Kim, C. Marvin Wayman, Precipitation reactions and strengthening behavior in 18wt Pct nickel maraging steels, *Metall. Trans. A* 21 (1990) 2655–2667.
- [33] O. Moshka, M. Pinkas, E. Brosh, V. Ezersky, L. Meshi, Addressing the issue of precipitates in maraging steels – Unambiguous answer, *Mater. Sci. Eng. A* 638 (2015) 232–239.
- [34] J.R. Scully, J.A. Van Den Avyle, M.J. Cieslak, A.D. Romig, C.R. Hills, The influence of palladium on the hydrogen-assisted cracking resistance of PH 13-8 Mo stainless steel, *Metall. Trans. A* 22 (1991) 2429–2444.
- [35] G.M. Pressouyre, Communications: A classification of hydrogen traps in steel, *Metall. Trans. A* 10 (1979) 1571–1573.
- [36] G.M. Pressouyre, I.M. Bernstein, A quantitative analysis of hydrogen trapping, *Metall. Trans. A* 9 (1978) 1571–1580.
- [37] W.Y. Choo, J.Y. Lee, Thermal analysis of trapped hydrogen in pure iron, *Metall. Trans. A* 13 (1982) 135–140.
- [38] H.G. Lee, J.Y. Lee, Hydrogen trapping by TiC particles in iron, *Acta Metall.* 32 (1984) 131–136.
- [39] J.Y. Lee, J.L. Lee, W.Y. Choo, Thermal analysis of trapped hydrogen in AISI 4340 steel, *Mater. Sci. Technol.* 17 (1983) 426–432.
- [40] S.M. Lee, J.Y. Lee, The effect of the interface character of TiC particles on hydrogen trapping in steel, *Acta Metall.* 35 (1987) 2695–2700.
- [41] M. Garet, A.M. Brass, C. Haut, F. Guttierrez-Solana, Hydrogen trapping on non metallic inclusions in Cr-Mo low alloy steels, *Corros. Sci.* 39 (1998) 1073–1086.
- [42] B.G. Pound, The effect of aging on hydrogen trapping in precipitation-hardened alloys, *Corros. Sci.* 42 (2000) 1941–1956.
- [43] N. Parvathavarthini, S. Saroja, R.K. Dayal, H.S. Khatak, Studies on hydrogen permeability of 2.25%Cr–1%Mo ferritic steel: correlation with microstructure, *J. Nucl. Mater.* 288 (2001) 187–196.
- [44] A. Turnbull, R.B. Hutchings, Analysis of hydrogen atom transport in a two-phase alloy, *Mater. Sci. Eng. A* 177 (1994) 161–171.
- [45] R.B. Hutchings, A. Turnbull, The effect of prior mechanical deformation on hydrogen transport through 13% chromium martensitic stainless steel, *Corros. Sci.* 33 (1992) 713–728.
- [46] A.M. Brass, J. Chene, Influence of deformation on the hydrogen behavior in iron and nickel base alloys: a review of experimental data, *Mater. Sci. Eng. A* 242 (1998) 210–221.
- [47] A.M. Brass, F. Guillon, S. Vivet, Quantification of hydrogen diffusion and trapping in 2. 25Cr-1Mo and 3Cr-1Mo-V steels with the electrochemical permeation technique and melt extractions, *Metall. Mater. Trans. A* 35 (2004) 1449–1464.
- [48] S. Frappart, X. Feaugas, J. Creus, F. Thebault, L. Delattre, H. Marchebois, Hydrogen solubility, diffusivity and trapping in a tempered Fe–Cr martensitic steel under various mechanical stress states, *Mater. Sci. Eng. A* 534 (2012) 384–393.